VTT Technical Research Centre of Finland

Evolution of alumina phase structure in thermal plasma processing

Kaunisto, Kimmo; Lagerbom, Juha; Honkanen, Mari; Varis, Tommi; Lambai, Aloshious;
Mohanty, Gaurav; Levänen, Erkki; Kivikytö-Reponen, Päivi; Frankberg, Erkka

Link to publication

Evolution of alumina phase structure in thermal plasma processing

Kimmo Kaunisto [a],[*], Juha Lagerbom [a], Mari Honkanen [b], Tommi Varis [c], Aloshious Lambai [c], Gaurav Mohanty [c], Erkki Levänen [c], Päivi Kivikytö-Reponen [a], Erkka Frankberg [c]

[a] *VTT Technical Research Centre of Finland Ltd, Tekniikantie 21, 02044, VTT, Espoo, Finland*
[b] *Tampere University, Tampere Microscopy Center, Korkeakoulunkatu 3, 33720, Tampere, Finland*
[c] *Tampere University, Materials Science and Environmental Engineering, Korkeakoulunkatu 6, 33720, Tampere, Finland*

ABSTRACT

Alumina (Al$_2$O$_3$) remains one the most important engineering ceramic for industrial applications. In addition to the α phase, transition alumina phases have interesting characteristics. Controlling the obtained phase structure from alumina melt requires processes with extreme cooling rates and therefore limits the tailoring capabilities. This study investigates how the cooling rate of pure alumina affects its microstructural properties and phase structure in plasma-based processing. The paper reports phase changes in micron sized granulated alumina particles in high-temperature plasma spheroidization and compares the results to plasma sprayed alumina coatings. Both plasma processes involve melting of the material followed by subsequent rapid cooling. Direct comparison on the alumina phase transitions is obtained for the two methodically distinct processing routes, creating unique microstructures due to difference in their cooling rates.

1. Introduction

Alumina possesses intriguing properties such as high hardness, resistant to abrasion, chemical inertness and low price, making it a tempting material for various applications [1,2]. To customize the performance of alumina, it is important to understand how the alumina characteristics can be controlled by heat treatment to improve its usability towards the desired applications.

As is well known, alumina exhibits several metastable phases, so-called "transition alumina phases", such as, gamma (γ), delta (δ), theta (θ), eta (η) and kappa (κ), in addition to the only thermodynamically stable alpha (α) phase [3]. Transition phases have different oxygen sub-lattices in face-centered cubic crystal (fcc) structure in comparison to the α phase with hexagonal close packed (hcp) structure, in which two-thirds of octahedral interstices are occupied with Al^{3+} cations. In transition phases, with the fcc crystal arrangement, oxygen anions and aluminum cations appear in many proportions with octahedral and tetrahedral configurations [4]. Identification of the transition alumina phases is a challenging task due to coexistence of phases, similarity of the phase structures and distorted crystal lattices. Phase transformation sequence from metastable alumina structures toward the stable α phase in heating is presented by Levin & Brandon [4].

The polycrystalline α phase is used, for example, in wear-resistant applications and cutting tools because of its high hardness and thermal stability. The metastable transition phases, such as γ, δ and θ are typically utilized, for example, as catalysts and catalysis support materials due to their lower surface energy and high specific surface area, respectively [5–7]. Controlled heating of alumina raw materials, such as boehmite (AlO(OH)), produces transition alumina phases as a function of temperature. γ-Alumina forms at the lowest temperature, around 300–500 °C, being stable below 700–800 °C. At higher temperatures γ transforms to δ and θ phases around 800–900 and 900–1100 °C, respectively, and finally to the stable α phase at around 1150 °C [3,5,8]. However, the alumina transformation highly depends on the heating rate and precursors used in the synthesis and hence only temperature range for each transition can be provided [5].

Transition alumina phases can be produced also using high temperature melting followed by solidification [9,10]. To avoid formation of the thermodynamically most stable α phase in the final material, quenching rate must be sufficiently high [11,12]. The γ forms predominantly in rapid cooling of melted alumina, being the path of least resistance among the alumina phases [11,13]. For obtaining specific crystallinity in plasma sprayed alumina, the cooling rate needs to be controlled. Cooling rate is also affected by substrate temperature and microstructures of isolated plasma sprayed alumina splats ranging from amorphous through γ crystallites to α alumina with the increase of the

substrate temperature from 573 K to 1173 K can be obtained [14]. Formation of amorphous phase from pure alumina demands even more extreme cooling rates in the order of 10^8–10^9 K/s [12]. Mixing of alumina with other substances, such as e.g. CaO or SiO_2, substantially facilitates the formation of the glassy phase [15,16]. According to Hashimoto et al. pure alumina is not a glass former in melt-quenching [16]. A related challenge is to produce single-phase transition alumina as the cooling rate should be similar throughout the whole material.

Earlier, few papers have been published considering the radio frequency (RF) -plasma treatment on ceramic raw-materials, typically Ca (OH)$_2$, or alumina powders [17–19]. These studies focus mostly on macroscopic characteristics of the materials upon the plasma treatment and less on microstructural features and phase transitions caused by the high-temperature processing and fast solidification. Therefore, the effect that high-temperature processing, followed by rapid cooling, has on the forming alumina phase structure, requires more attention to allow achieving material properties that are optimal for the chosen application, for example in thermal sprayed alumina coatings. In contrast to RF-plasma, direct current (DC)-plasma spraying of alumina coatings is commonly used commercially. The plasma sprayed alumina coatings has often reported to contain γ, α and amorphous phases, α being at least partly unmolten or partially molten particles [20–24]. Typically, no η phase has been detected in thermal sprayed coatings although Zhou et al. has documented occurrence of η phase in alumina [25].

In this paper, we study alumina phase transitions in rapid melt solidification. We compare alumina phase structures obtained in two similar processing technologies, RF-plasma spheroidization (particle cooling rate approx. 10^6 K/s [26] and plasma spray coating (particle cooling rate approx. 10^8 K/s [27], to understand the phase structure complexity prevailing after the thermal processing steps. Furthermore, microstructures of the powder particles and coating are investigated using the electron backscatter diffraction (EBSD) technique. The EBSD study reveals the dynamic nature of the heat treatments by showing that the heat-treated alumina microstructure is a combination of multiple phases rather than a single-phase structure. Phase evolutions of pure α-alumina powder during the RF-plasma spheroidization and in plasma sprayed coating are compared and discussed.

The motivation for this study was to gain a better understanding of the phase transitions between the metastable phases and α phase that occur during rapid solidification of pure alumina. This sheds light on the microstructural changes that might take place during the processing of alumina, which potentially has a significant effect on the materials properties and performance. The EBSD mapping is used to report phase structure and grain orientations within individual particles, which are compared to the phase structure of a plasma sprayed alumina coating, providing new knowledge to the scientific community.

2. Materials and methods

As received, pure alumina powder Metco 6103 (>99.98%, Oerlikon Metco) was used as a raw material in this study. The main impurities were Ca (30 ppm), K (27 ppm), Na (40 ppm), Fe (41 ppm) and Si (40 ppm). The measured particle size distribution of this reference powder was D_{10} = 19 μm, D_{50} = 31 μm and D_{90} = 50 μm. The powder particles have been manufactured by spray drying and sintering method from fine grained primary particles causing the porous microstructure of the powder particles. The porous structure is formed when the primary particles attach to each other by necking in sintering, as only partial densification is aspired.

Particle morphologies were studied by scanning electron microscopy (SEM, JSM-636OLV, JEOL and ULTRA plus Thermal Field Emission Scanning Electron Microscope, Carl Zeiss Microscopy GmbH). The cross-sectional powder and coating samples were prepared with a standard metallographic sample preparation method that includes molding of the powder/coating into a resin, followed by polishing of the sample surface.

Qualitative phase analyses were carried out by an X-ray diffractometer (XRD, Empyrean, PANalytical B.V.) with Cu-Kα radiation source and analyzed using the HighScore Plus software with the ICDD crystallographic database.

A differential scanning calorimetry (DSC) function of a thermogravimetric analysis instrument STA 449 F1 Jupiter (Netzch Group) was used to investigate heat induced phase transitions of the powders and coating. For the DSC experiments, samples of about 30 mg were analyzed with a heating rate of 10 K/min from 40 to 1300 °C, with no holding times, in an inert N_2 atmosphere. In the case of plasma sprayed coating, the DSC measurement was performed using a piece of coating detached from the steel substrate.

A RF induction-plasma spheroidizator (Tekna Teksphere 15, Tekna Holding AS) was used for the plasma treatment of the powder studied. Argon was used as both carrier and sheathing gas in the process. A stable plasma was generated by switching on an RF induction after evacuation the processing chamber and starting the argon purge. During the operation, alumina powder particles were fed axially into the plasma zone through a powder feeder. The high temperature in the plasma zone melted the powder particles, forming liquid droplets under the action of surface tension. These droplets, when they fly out of the plasma zone, rapidly solidified to form spherical particles. The powder was collected using a water-cooled steel vessel under the processing chamber. In this work, the plasma operated at a frequency of 4 MHz and a power of 15 kW using powder feed rate of 9 g/min. The collected powder was washed by ethanol to remove nanosized particles that typically appear on the surface of the powder particles because of evaporation and solidification some of the raw material during the plasma spheroidization due to its very high temperature.

Plasma spray coatings were deposited using a direct current plasma spray system (Sulzer Metco A3000S, OC Oerlikon Corporation AG) equipped with a F4-MB plasma gun with unaxial powder feeder. In plasma spraying, particle velocities typically are in order of 150–400 m/s. Particle temperatures can be as high as 2000–4000 °C due to very high plasma temperature [28]. The coating was deposited onto a 5 mm thick steel plate. The coating was sprayed with Ar and H_2 at flow rate of 43 and 14 l/min, respectively, using 50 kW power, spraying distance of 110 mm and powder feed rate of 17 g/min.

The main differences between the two plasma equipment are the plasma generation method (radio frequency induction and direct current between electrodes), plasma gas velocity and powder feed system. Both methods operate in the same order of plasma gas flow rates, but in DC plasma spray, the gas is accelerated through a small cavity and nozzle to a considerably higher velocity. Furthermore, in plasma spheroidization, the particles are cooled down in the gas atmosphere, while in plasma spraying, the particles are cooled down faster when they hit the substrate surface. Both plasma processing methods are illustrated in Fig. 1. Similar carrier gas powder feeders are used, but coaxially in the plasma spheroidization and non-axially in the plasma spraying.

Crystallographic information of samples was obtained by electron backscatter diffraction (EBSD) technique. The EBSD system (Symmetry, Oxford Instruments plc) is integrated in a FE-SEM ULTRAplus (Carl Zeiss Microscopy GmbH). In the EBSD measurements, the acceleration voltage of 15 kV and the step sizes of 0.25 μm and 0.1 μm were used. The EBSD data was collected by the AZtec software and processed using the CHANNEL5 software (both from Oxford Instruments). In the EBSD results, a band contrast (BC) map shows the quality of the Kikuchi diffraction pattern for each measurement pixel: bright means that the pattern quality is good, and it can be indexed and black signifies that the pattern quality is poor. The colors in the EBSD inverse pole figure (IPF) maps (z direction) correspond to the crystallographic orientations as indicated by a colored stereographic triangle. Powder samples and a cross-sectional sample from the plasma-sprayed coating (using reference powder) for the EBSD measurements were prepared with the standard metallographic method. A final polishing and carbon coating were carried out by a cooling cross-section polisher (CCP, B–19520CCP,
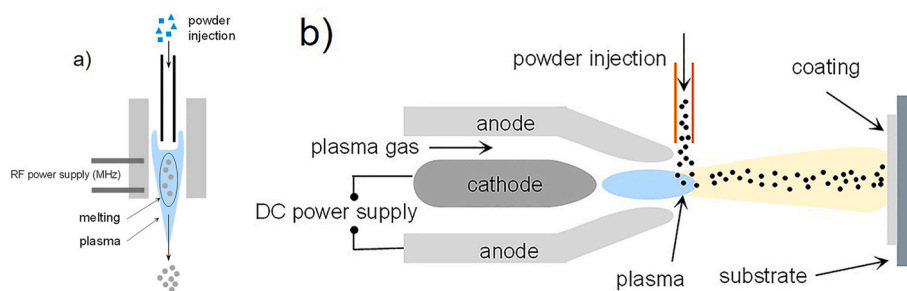
Fig. 1. Schematic illustrations of a) RF-plasma spheroidization and b) DC plasma spraying.

JEOL). The carbon coating was deposited to avoid sample charging during the EBSD measurements.

Nanoindentation tests were performed on the spherical alumina powders in both as-received and plasma spheroidized conditions to determine differences in their mechanical properties. An Alemnis in-situ nanoindenter (Alemnis AG, Switzerland) was used inside a Zeiss LEO 1450 SEM to perform indentation tests on the alumina powder particles individually. A cube corner tip (Synton SDP, Switzerland) made of electrically conductive diamond was used for these experiments. The use of in-situ nanoindentation inside the SEM allows precise positioning of the indenter tip on the top surface of each powder particle such that the indentation can occur on relatively flat surface (see Supplementary Information, Fig. S1). The positioning accuracy of the Alemnis nanoindenter in XYZ is < 5 nm. The indentation profile comprised of the following segments (i) loading in displacement-controlled mode at 25 nm/s up to a load target of 40 mN, (ii) hold the load constant at 40 mN for 30 s, (iii) unload to zero displacement (starting displacement at the beginning of the test) in displacement-controlled mode at 25 nm/s. The indenter allows mixing both displacement-controlled [29] and load-controlled segments in an indentation profile. The indenter tip was cleaned after each indent by performing deep indents (~5 μm depth) on a piece of copper. A minimum of 6 indentation tests were performed on each alumina type: as-received and plasma spheroidized. The load-displacement curves from each indent were analyzed using method [30] to extract hardness and modulus values.

3. Results

X-ray diffraction measurements were performed to identify the obtained average phase structures of the alumina powder and coating after the high-temperature plasma spheroidization and plasma spraying, respectively (Fig. 2). In the both methods, the powdery raw-material melts at a high-temperature, at least partly, and then solidifies rapidly.

The as-received alumina powder shows only α phase (Fig. S2). The XRD pattern of the high-temperature plasma spheroidized powder (Fig. 2b) shows peaks for α phase (ICDD 04-007-1400) and transition phases δ (ICDD 04-008-4095), θ (ICDD 016–0394) and γ (ICDD 029–0063). The phase composition is similar to the previously reported phase structure of plasma spheroidized alumina [31]. Fig. 2b presents XRD pattern for the plasma sprayed alumina coating with thickness of about 380 μm. The XRD pattern of the coating shows peaks for α and γ transition phase. These are the two phases typically assumed to be formed in thermal spray coating of alumina [20–22]. The XRD baseline of the coating pattern is not flat indicating there are some nanocrystalline and/or deformed crystal lattices present as is typical for the given coating deposition method. The XRD data of either plasma process shows no indication of the presence of glassy Al_2O_3 (no broad hump around $2\theta = 20$–$40°$) despite the fast cooling that occurs after the plasma torch.

X-ray diffraction analyses of the plasma sprayed alumina coating after heat treatments at 900, 1100 and 1300 °C were performed to support conclusions on the alumina phase transitions (Fig. S3) As
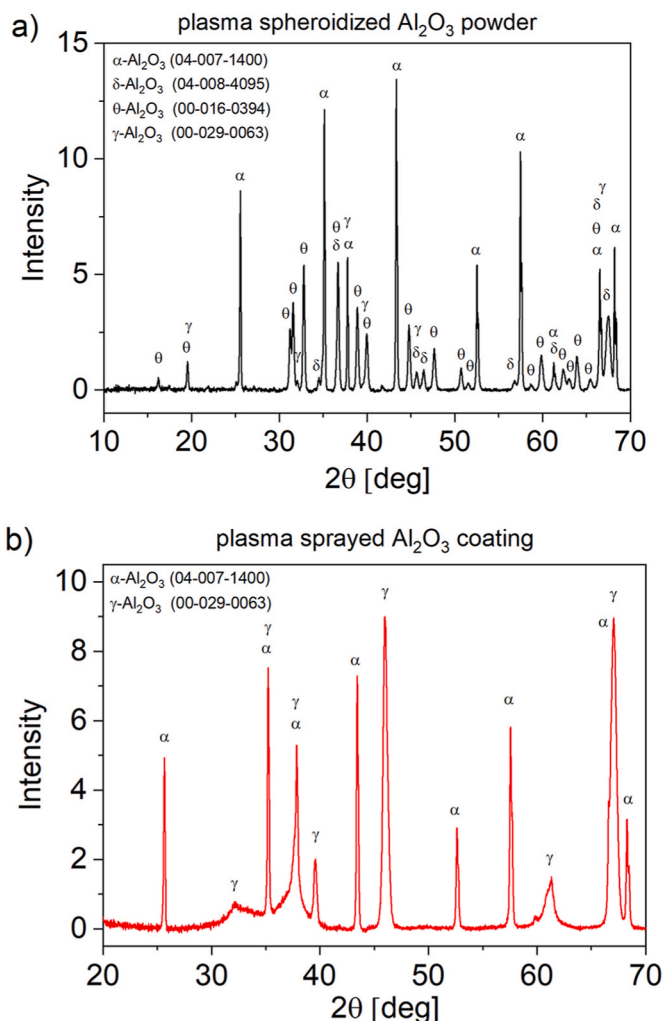

Fig. 2. XRD patterns of the a) plasma spheroidized alumina powder and b) plasma sprayed alumina coating. The as-received alumina powder was used for both processes.

discussed earlier, the as-sprayed alumina coating shows only α and γ with no other transition alumina phases. After the heat treatment at 900 °C, the diffraction peaks of δ phase appear showing the γ to δ transition. Transition of γ to δ phase, around 800–900 °C, is not complete due to the insufficient heat treatment time. Transition of δ to θ phase takes place around 900–1100 °C and only θ and α peaks are present after the heating up to 1100 °C. The θ peaks show only weak diffraction peaks due to the small sample size used. However, the transition to θ is obvious as γ and δ peaks are no longer visible. After the heat treatment up to 1300 °C, only α peaks are present (the θ to α

transition takes place around 1150 °C).

We studied the effect of the high-temperature plasma treatment, followed by rapid cooling, on the alumina particle microstructures and crystallography, using SEM together with EBSD prior and after the plasma spheroidization. Fig. 3 presents the SEM images of the alumina particles before and after the plasma spheroidization treatment. As shown in the figure, the spray-dried porous alumina particles have solidified into dense spheres in the high-temperature plasma processing. Therefore, the temperature prevailing in the plasma was high enough to completely melt the α particles.

Fig. 3e and f shows the cross-sectional SEM image of the plasma sprayed alumina coating. SEM imagining was performed to study the microstructure of the coating to more comprehensively understand the microstructure that forms during the coating deposition. The coating appears dense with some micro-cracks and splat boundaries from particle flattening upon high-speed impact to the substrate. The round dark areas represent local porosity being trapped in the coating structure. In addition, few areas having original particle-type porous structure were observed indicating insufficient particle melting during the deposition.

According to the EBSD maps collected from the particle cross-sections (Fig. 4), the as-received spray-dried alumina particles are fully α phase with spherical grains and with the grain size of 1.1 ± 0.2 μm (determined from the EBSD data by Channel 5 software). Instead, the plasma-spheroidized particles contain various phases with irregular grain size and morphology (Fig. 5). EBSD maps collected from the individual plasma-spheroidized particles are presented in Fig. 6 α-rich particles with irregular grains (Fig. 6a) and θ-rich particles with mainly elongated grains (Fig. 6b) were observed. In addition, particles with a mixture of α phase (both melt solidified and unmolten) and transition phases θ, δ, and γ with irregular grains (Fig. 6c) were detected. There

were also particles containing a mixture of the three transition phases (Fig. 6d) where in the θ phase has mainly elongated grains while the δ and γ phases have irregular grain morphology. As shown in Fig. S4, porous α phase particles, similar to the as-received powder, were found to remain in the powder, which indicates that these particles did not pass through the high-enough temperature zone in the plasma to melt these particles. The microstructure of the particles after the plasma treatment most likely differs from each other due to a slight difference in plasma exposure time or temperature for individual particles.

Fig. 7 shows EBSD maps of the plasma-sprayed alumina coating sprayed using the as-received alumina powder. There are α- and γ-rich areas and areas that were not identified (grey areas). The α phase has mainly spherical grains with the size of 1.2 μm ± 0.4 (determined from the EBSD data by Channel 5 software) corresponding the original particle-type structure (Fig. 5b). While the γ phase has irregular grain morphology. Transition phases γ, δ, θ, and η were studied but only γ was detected.

High-temperature DSC characterization was performed to further study the heat induced phase transitions in the plasma spheroidized alumina powder and the plasma sprayed alumina coating (Fig. 8). The plasma-spheroidized powder shows a weak exothermic phase transition from δ to θ around 950 °C. An exothermic peak around 1120 °C corresponds to the phase transition from the θ to α [8]. In the case of the plasma spheroidized powder, we observed no visible peaks corresponding to the γ to δ (around 800–900 °C). These observations suggest that the most dominant transition phase formed during the plasma spheroidization treatment is the θ phase. The γ phase observed in EBSD analysis is not visible in the DSC due to its minor quantity, which is in line with the XRD experiments. The as-received powder does not show any phase transition within the temperature range because it consists of
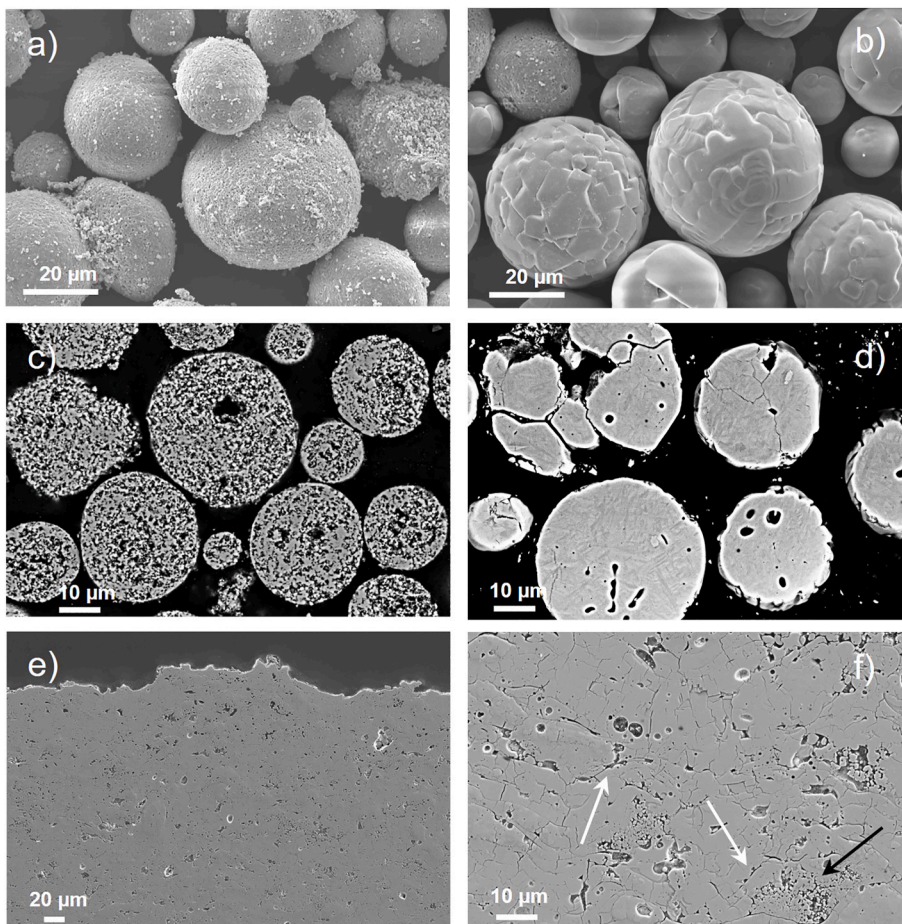

Fig. 3. Surface morphology (a, b) and cross-sectional (c, d) SEM images of alumina powder prior (a, c) and after (b, d) the plasma spheroidization. In Fig. 3c and d, the black colored areas are porosity. In Fig. 3e and f, cross-section SEM images of the plasma spray deposited alumina coating are presented with two magnifications. The as-received alumina powder was used for the coating deposition. In Fig. 3f, white arrows show examples of splat boundaries, and black arrow an example of an un-melted particle in the coating.
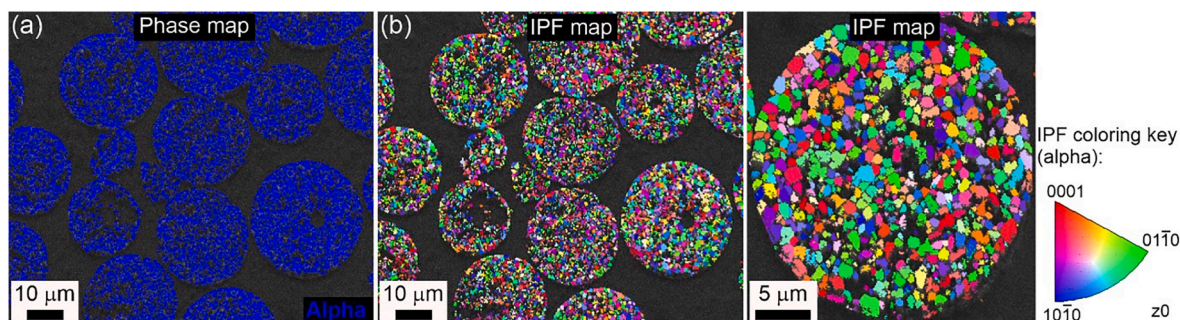
Fig. 4. EBSD maps of the as-received alumina powder, (a) the phase map superimposed on the band contrast map for a collection of particles showing fully α-phase and (b) inverse pole figure (IPF) maps superimposed on the band contrast maps for a collection of particles and an individual particle (including the IPF coloring key) showing grain orientations and their morphology. Areas colored shades of grey represent the original Band contrast map and are not indexed in the IPF map. (For interpretation of the references to color in this figure legend, the reader is referred to the Web version of this article.)
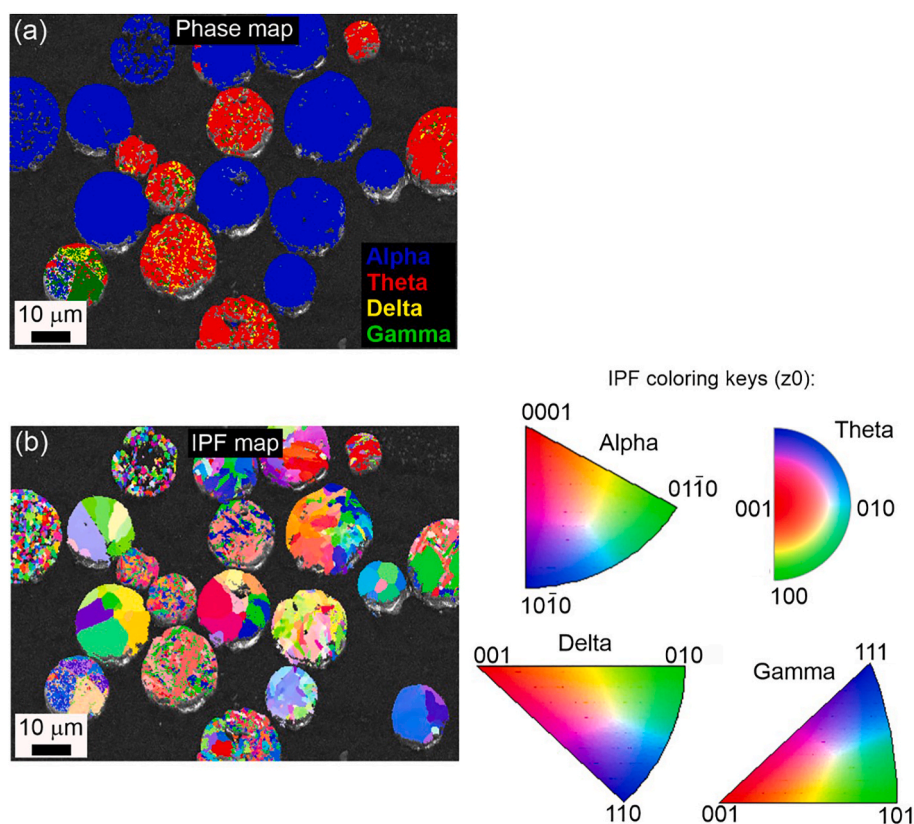

Fig. 5. EBSD maps of a collection of the high-temperature plasma spheroidized alumina particles, (a) the phase map superimposed on the band contrast map showing particles with various phases and (b) the inverse pole figure (IPF) map superimposed on the band contrast map (including the IPF coloring keys) showing grain orientations and their irregular size and morphology.

the thermodynamically stable α phase (Fig. S5).

The DSC results for the plasma sprayed coating show the phase transition from γ to δ at 850 °C, which was not visible with the plasma spheroidized powder. This is due to the significantly higher relative amount of γ in the as-sprayed plasma sprayed coating in comparison to the plasma spheroidized powder, as supported by the XRD and EBSD. In addition, the plasma sprayed coating similarly shows exothermic peaks around 980 and 1150 °C, corresponding to the phase transitions from δ to θ and θ to α, respectively. The small shift in transition temperatures of 30 °C compared to the plasma spheroidized powder is assumed to be due to crystal defects and deformations in the coating that slightly change the phase transition energies.

Finally, to demonstrate how the plasma treatments have the potential to significantly change the perceived material properties towards a

selected application, we performed nanoindentation on singular as-received and the plasma spheroidized particles. Nanoindentation load-displacement curves obtained from as-received and plasma spheroidized alumina particles are shown in Fig. S6. Several load-drops in the loading curves are observed in both cases. The as-received particles show higher frequency and larger magnitude of load-drops compared to the plasma spheroidized particles. The load drops observed with the as-received powder can be explained by the porous structure of the particles, i.e., the load drops occur when the necks connecting the primary particles break) (Fig. 3c). The average hardness and Young's modulus values calculated from the nanoindentation results are presented in Table 1 for both particle types, being about 2-times greater for the plasma spheroidized alumina particles. The densified plasma spheroidized particles show smoother nanoindentation curves as no cracks were
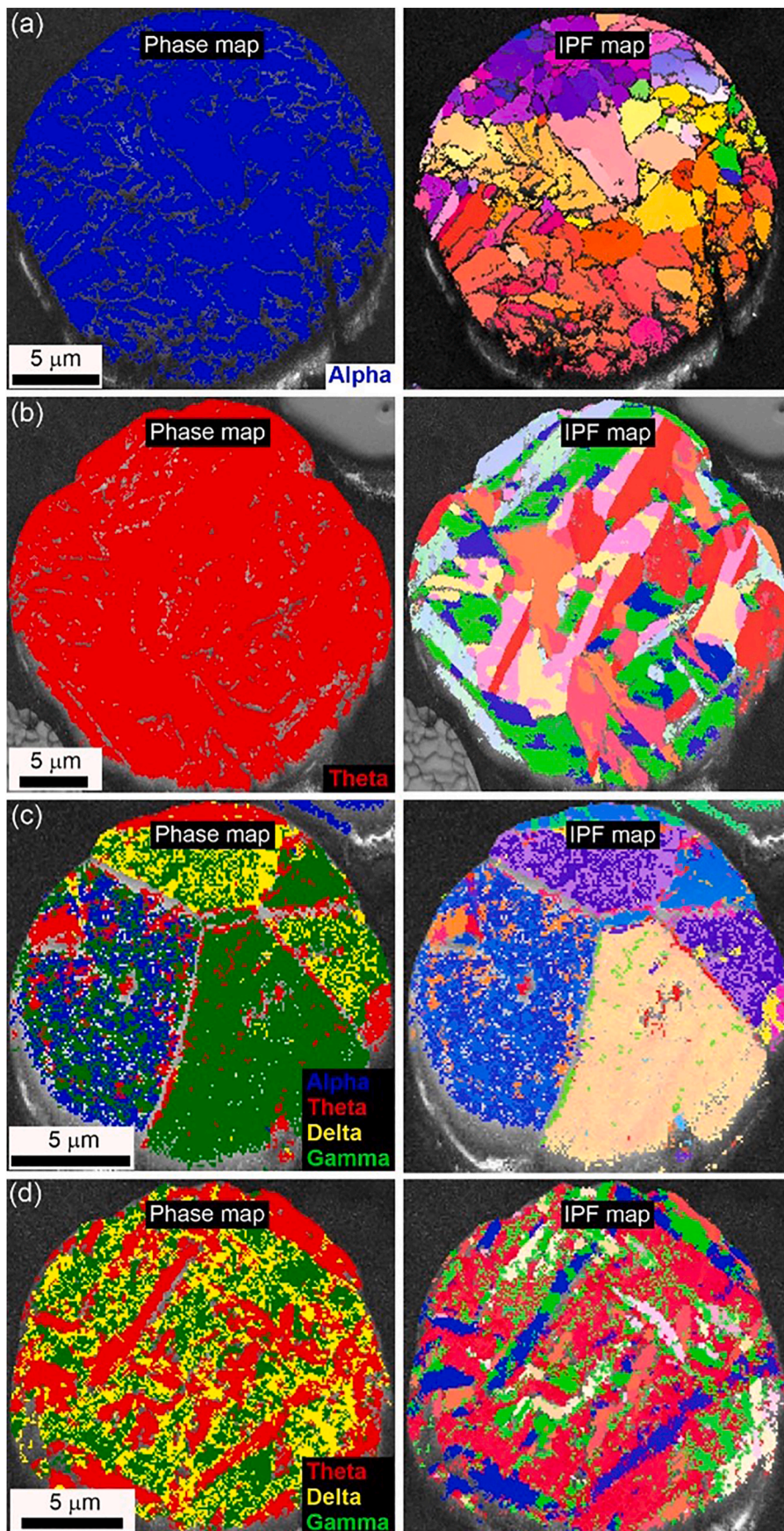
Fig. 6. EBSD maps of individual particles of the high-temperature plasma spheroidized alumina particles. The phase map superimposed on the band contrast map shows phases existing in the particles and the inverse pole figure (IPF) map superimposed on the band contrast map shows grain orientations, (a) An α-rich particle with irregular grains, (b) a θ-rich particle with mainly elongated grains, (c) a particle with a mixture of α phase and transition phases θ, δ, and γ with irregular grains, and (d) a particle with a mixture of transition phases θ, δ, and γ; the θ phase having mainly elongated grains while the δ and γ phases have irregular grain morphology. IPF coloring keys presented in Fig. 5b.
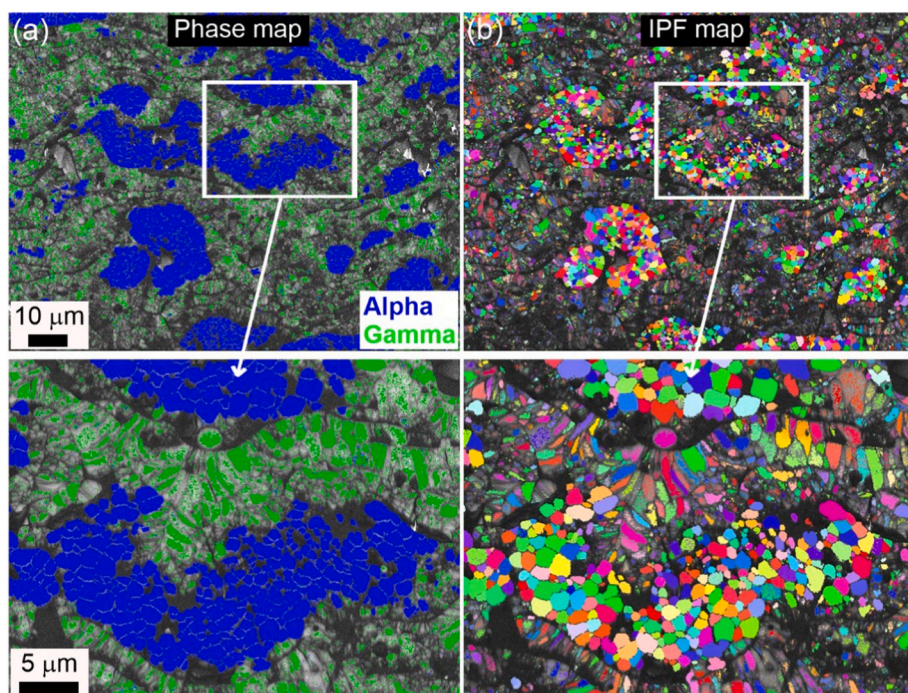
Fig. 7. EBSD maps with two magnifications of the plasma-sprayed alumina coating. (a) Phase maps superimposed on the band contrast maps show the distribution of α and γ phases and (b) inverse pole figure (IPF) maps superimposed on the band contrast maps (show that α-phase has mainly spherical grains while the γ phase has irregular grains morphology. IPF coloring keys for α and γ phases presented in Fig. 5. Areas colored shades of grey represent the original Band contrast map, and are not indexed in the IPF map. (For interpretation of the references to color in this figure legend, the reader is referred to the Web version of this article.)
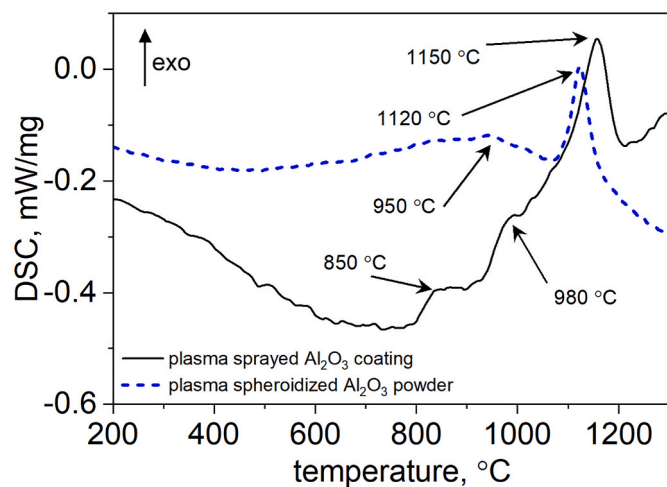

Fig. 8. DSC characterization of the plasma spheroidized alumina powder and plasma sprayed alumina coating. The phase transitions verified by XRD are indicated by arrows in the figure.

Table 1
The hardness and modulus values of the as-received and plasma spheroidized alumina particles.

	as-received	plasma spheroidized
Hardness (GPa)	13.3 ± 4.2	27.3 ± 8.8
Young's modulus (GPa)	97.2 ± 22.5	207.2 ± 62

observed in the measurements. The higher hardness and Young's modulus values observed for plasma spheroidized particles, although the load-displacement results show substantial scatter for both powder types, indicate that as-received particles has densified during the plasma spheroidization. The detailed phase structure of the studied particles in nanoindentation is unknown and hence mechanical properties of the different alumina phases cannot be identified, however, the large

deviation in the data can be explained by the rich variety of different phase structures observed in the plasma spheroidized particles by EBSD and other supporting techniques.

4. Discussion

The alumina transition phases that appear after solidification are strongly affected by the cooling rate following the solidification sequence of gamma-delta-theta-alpha, from cold to hot end, i.e., following the same crystallization sequence compared to the thermal decomposition of boehmite to alumina when heated. In the plasma spheroidized powder, the low amount of γ, indicated by the relatively low intensity of X-ray peaks for γ, was not foreseen, as the γ is typically the dominant phase present in thermal sprayed alumina coatings, as also shown by the results here, when experiencing the rapid cooling after hitting the relatively cool substrate surface. This indicates that the cooling rate in plasma spheroidizing treatment, in which particles cool down in a hot gas atmosphere, was lower compared to the plasma spraying (still rapid enough to induce transition alumina phases). More rarely identified transition phases κ or η were not found in this study. Furthermore, no glassy phase was detected because of too slow cooling rate or since the volume of amorphous phase was too low to be detected by XRD and DSC. The tendency to form a glass phase can be significantly increased by alloying, but chemically pure alumina, as in this case, requires very fast solidification and cooling rates.

Identification of the transition alumina phases is known to be difficult merely by XRD due to the overlapping of the corresponding diffraction peaks. For this reason, XRD cannot solely be used for phase identification and the results must be verified using additional methods. In this paper, EBSD method was used as a parallel identification method. With the combined characterization, alumina transition phases were detected in the material after both plasma-based processing methods. Only γ and α phases were observed in the plasma sprayed coating in comparison to the plasma spheroidization, where δ and θ phases were present, together with γ and α. That is, the phase composition of plasma spheroidized particles and plasma deposited coating measured by XRD are in line with the EBSD phase identification.

Based on the phase analysis results, the cooling rate in the plasma

spraying seems to be notably higher, which leaves the structure dominantly in γ phase. In the literature, particle cooling rates of 10^6 K/s [26] and 10^8 K/s [27,32] are associated with the plasma spheroidization and plasma spraying methods, respectively. Therefore, it can be assumed that cooling rate must be at least 10^6 K/s to produce any other transition phases (δ and θ), and close to 10^8 K/s to form γ phase. α alumina seeding is known to reduce the transition temperature for α [33,34] and, as shown by plasma spraying treatments, it is possible that some crystalline α phase remains in the structure during the plasma processing as a result of the seeding [35] or the solid-state γ to α phase transformation [36,37] That is a plausible explanation why the structure has both γ and α phase, but no other transition phases were detected. Moreover, it is generally accepted that in solidification on impact, molten alumina nucleates to γ phase if the droplet in fully melted because of the low interfacial energy involved in γ nucleation [11,35].

Amorphous alumina becomes metastable at cooling rates of about 10^8–10^9 K/s [12], i.e. cooling rate in plasma spraying is close to the cooling rate required to retain the amorphous structure. However, again the presence of crystalline seed phases in the cooling material and low interfacial energy of γ nucleation can enable homogeneous crystallization with higher cooling rates due to epitaxial crystallization occurring at lower activation energy. According to Gualtieri et al., the amount of amorphous phase in the plasma sprayed alumina coating may be around 10% be weight determined by the Rietveld refinement [38]. No amorphous phase was identified in the plasma sprayed coatings in this study. However, ultra-pure alumina was used in this study that potentially further decreases formation of the glassy phase. The microstructure and phase content of thermal sprayed alumina coatings has shown to depend on the coating process parameters and fraction of transition phases can be close to 100% if particle melting is good [2,35,39,40].

α phase was identified after both the plasma spheroidization and the plasma spraying, which is partly due to a small number of unmolten particles passing through to the end-product in both processing methods. As evidence of this, un-molten α-particles were detected both in the coating cross-section imagining (Fig. 3) and plasma spheroidizing (Fig. S4). In the case of plasma spheroidized powder, the densified particles having α phase have experienced slower cooling rates due to slightly different heating-cooling cycle, as the plasma torch has a temperature distribution along the cross-sectional radius of the plasma. This signifies the need of process optimization when using plasma spheroidization.

Alumina phases in the plasma spheroidized powder were identified with XRD and EBSD, however, in the case of plasma sprayed coating, there were also non-indexed areas in the EBSD maps (Fig. 7). These areas mainly located at the splat boundaries and no entirely non-indexed splats were observed. Being a dynamic process, plasma spraying induces crystal deformations during solidification (shrinking, residual stresses) that might hinder phase identifications in XRD and EBSD [41]. Nanosized, deformed, amorphous and porous areas exist as non-indexed areas in the EBSD maps. Since no other phases, excluding γ and α, were detected either by XRD or EBSD, it is likely that there are no other transition phases present in the plasma sprayed coating, which is line with the previous literature [20,21]. Due to the non-indexed areas in EBSD and peak overlapping in XRD, no reliable phase quantification could be calculated.

Two different types of α particles were identified among the plasma spheroidized powder. The first type α particles resembled the as-received alumina particles and were α phase likely because they did not melt at all, when subjected to the plasma hot zone. The solid α-particles clearly melted during the plasma spheroidization treatment but went through a slower cooling, enabling solidification to α phase. Furthermore, the EBSD reveals that a large diversity of phases and grain morphology can be present after plasma spheroidization, which should be considered when planning such a processing for a certain application. Some particles showed a diverse mixture of phases, including δ, θ and α phases due to rapid cooling. The particles with the smallest particle size, which had a faster cooling rate than the larger particles, therefore consisted mostly of transition phases, indicating that the cooling rate in the plasma spheroidization treatment reached a threshold that allowed solidification into transition phases, instead of α phase. The larger grains were typically α, although the α phase coexisted with transition phases having a smaller grain size within the same particle, indicating a slightly slower cooling rate in relation to the smaller particles.

In previous studies, hollow ceramic microspheres are formed during plasma treatment of porous raw materials instead of densified particles presented in this study [42,43]. The formation of hollow structure is related to the non-uniform melting of particles forming a gas cavity and a spherical cell. This is related to low temperature plasma where gradient melting of particles traps the pore gas within the molten surface layer. In this study, high-temperature plasma treatment caused gradient-free heating of the particles, which allowed gas escape during melting and thus the formation of densified particles with some distributed closed-type porosity (Fig. 3d). Furthermore, agglomerated and sintered powder that was used as a starting material may have a high enough density to prevent the formation of a hollow structure but allow the formation of a densified structure with distributed closed-type porosity.

Finally, the hardness and Young's modulus values obtained for single plasma spheroidized particles give an indication that the plasma treatment not only densifies the structure, indicated by marked increase in the hardness and Young's modulus, but in addition can result in a variety of different mechanical properties depending on the prevailing process conditions, as indicated by the large deviation in the results. However, it was not possible to target the nanoindentation measurements to particles with a defined single-phase structure in order to compare the physical properties of the transition phases.

In other words, by carefully monitoring the process conditions, the functionality of alumina can be extended even to new applications, even though alumina is a well-established engineering material.

5. Conclusions

We have shown that the plasma spheroidization coupled with electron backscatter diffraction and supporting methods, allow an effective route to study the intermediate transition phases produced in dynamic melt-quenching processes of alumina and giving new insight on how to control plasma spraying process and the achieved microstructure. The study reveals that the alumina phase structure could be affected by the plasma processing parameters even in the case of pure alumina and that a rich variety of phase compositions is reached by changing the cooling rate of the melt.

Based on the current results, it seems possible to selectively fabricate a tailored phase composition according to the cooling profile that the alumina particles undergo in the plasma treatment. This further addresses the importance of the cooling rate on alumina phase structure and hence on its properties. That is, alumina cooling rate must be considered in applications where the surface properties play a crucial role.

By changing the cooling profile of the plasma process, the obtained alumina phase composition can be ideally adjusted for specific functionality, such as phase composition, porosity and mechanical properties that are suitable for a large variety of engineering applications. Further studies should focus on technical aspects of how to accurately measure and control the particle cooling rate during thermal processing to produce the desired alumina phase structure for the end-product. Customized phase structures would expand the usability of such materials in a wider range of applications. Transition alumina powders with optimized phase structure could be used as a catalyst bed material in chemical gas phase reactors. Highly corrosive environments on the other hand require materials with no transition phases as α phase possesses the highest stability among the alumina phases.

Declaration of competing interest

The authors declare that they have no known competing financial interests or personal relationships that could have appeared to influence the work reported in this paper.

Acknowledgements

Appendix A. Supplementary data

Supplementary data to this article can be found online at https://doi.org/10.1016/j.ceramint.2023.03.263.

References

[1] A.M. Abyzov, Aluminum oxide and alumina ceramics (review). Part 1. Properties of Al_2O_3 and commercial production of dispersed Al_2O_3, Refract. Ind. Ceram. 60 (2019) 24–32, https://doi.org/10.1007/s11148-019-00304-2.

[2] S.T. Aruna, N. Balaji, J. Shedthi, V.K.W. Grips, Effect of critical plasma spray parameters on the microstructure, microhardness and wear and corrosion resistance of plasma sprayed alumina coatings, Surf. Coating. Technol. 208 (2012) 92–100, https://doi.org/10.1016/j.surfcoat.2012.08.016.

[3] A. Boumaza, L. Favaro, J. Lédion, G. Sattonnay, J.B. Brubach, P. Berthet, A. M. Huntz, P. Roy, R. Tétot, Transition alumina phases induced by heat treatment of boehmite: an X-ray diffraction and infrared spectroscopy study, J. Solid State Chem. 182 (5) (2009) 1171–1176, https://doi.org/10.1016/j.jssc.2009.02.006.

[4] I. Levin, D. Brandon, Metastable alumina polymorphs: crystal structures and transition sequences, J. Am. Ceram. Soc. 81 (8) (1998) 1995–2012, https://doi.org/10.1111/j.1151-2916.1998.tb02581.x.

[5] L. Kovarik, M. Bowden, J. Szanyi, High temperature transition aluminas in δ-Al_2O_3/θ-Al_2O_3 stability range: review, J. Catal. 393 (2021) 357–368, https://doi.org/10.1016/j.jcat.2020.10.009.

[6] M. Trueba, S.P. Trasatti, γ-Alumina as a support for catalysts: a review of fundamental aspects, Eur. J. Inorg. Chem. 2005 (17) (2005) 3393–3403, https://doi.org/10.1002/ejic.200500348.

[7] G. Busca, Silica-alumina catalytic materials: a critical review, Catal. Today 357 (2020) 621–629, https://doi.org/10.1016/j.cattod.2019.05.011.

[8] S. Lamouri, M. Hamidouche, N. Bouaouadja, H. Belhouchet, V. Garnier, G. Fantozzi, J.F. Trelkat, Control of the γ-alumina to α-alumina phase transformation for an optimized alumina densification, Bol. Soc. Espanola Ceram. Vidr. 56 (2) (2017) 47–54, https://doi.org/10.1016/j.bsecv.2016.10.001.

[9] R. McPherson, On the formation of thermally sprayed alumina coatings, J. Mater. Sci. 15 (1980) 3141–3149, https://doi.org/10.1007/BF00550387.

[10] R. McPherson, The structure of Al_2O_3-Cr_2O_3 powders condensed from a plasma, J. Mater. Sci. 8 (1973) 859–862, https://doi.org/10.1007/BF00553736.

[11] L. Marcinauskas, P. Valatkevicius, The effect of plasma torch power on the microstructure and phase composition of alumina coatings, Materials Science-Poland 28 (2) (2010) 451–458.

[12] C. Pan, P. Shen, S.-Y. Chen, Condensation, crystallization and coalescence of amorphous Al_2O_3 nanoparticles, J. Cryst. Growth 299 (2) (2007) 393–398, https://doi.org/10.1016/j.jcrysgro.2006.12.006.

[13] R. McPherson, The relationship between the mechanism of formation, microstructure and properties of plasma-sprayed coatings, Thin Solid Films 83 (3) (1981) 297–310, https://doi.org/10.1016/0040-6090(81)90633-7.

[14] E.-J. Yang, X.-T. Luo, G.-J. Yang, C.-J. Li, M. Takahashi, S. Kuroda, K.H. Kim, Impact of deposition temperature on crystalline structure of plasma-sprayed Al_2O_3 splats revealed by FIB-HRTEM technique, Ceram. Int. 42 (1) (2016) 853–860, https://doi.org/10.1016/j.ceramint.2015.09.010.

[15] M. Ozabaci, M.A. Aksan, G. Kirat, O. Kizilaslan, M.E. Yakinci, Preparation and characterization of CaO-Al2O3-SiO2 (CAS) glass-ceramics, J. Non-Cryst. Solids 454 (2016) 8–12, https://doi.org/10.1016/j.jnoncrysol.2016.10.019.

[16] H. Hashimoto, Y. Onodera, S. Tahara, S. Kohara, K. Yawaza, H. Segawa, M. Murakami, K. Ohara, Structure of alumina glass, Sci. Rep. 12 (2022) 516, https://doi.org/10.1038/s41598-021-04455-6.

[17] V. Chaturvedi, P.V. Ananthapadmanabhan, Y. Chakravarthy, S. Bhandari, N. Tiwari, A. Pragatheeswaran, A.K. Das, Thermal plasma spheroidization of aluminum oxide and characterization of the spheroidized alumina powder, Ceram. Int. 40 (6) (2014) 8273–8279, https://doi.org/10.1016/j.ceramint.2014.01.026.

[18] Z. Károly, J. Szépvölgyi, Plasma spheroidization of ceramic particles, Chem. Eng. Process: Process Intensif. 44 (2) (2005) 221–224, https://doi.org/10.1016/j.cep.2004.02.015.

[19] Z. Károly, J. Szépvölgyi, Z. Farkas, Simultaneous calcination and spheroidization of gibbsite powders in an RF thermal plasma, Powder Technol. 110 (3) (2000) 169–178, https://doi.org/10.1016/S0032-5910(99)00195-3.

[20] S. Valette, R. Bernardie, J. Absi, P. Lefort, Elaboration and characterisation of plasma sprayed alumina coatings on nickel with nickel oxide interlayer, Surf. Coating. Technol. 416 (2021), 127159, https://doi.org/10.1016/j.surfcoat.2021.127159.

[21] S. Guanhong, H. Xiaodong, S. Jiuxing, S. Yue, Parametric study of Al and Al_2O_3 ceramic coatings deposited by air plasma spray onto polymer substrate, Appl. Surf. Sci. 257 (17) (2011) 7864–7870, https://doi.org/10.1016/j.apsusc.2011.04.057.

[22] E.J. Young, E. Mateeva, J.J. Moore, B. Mishra, M. Loch, Low pressure plasma spray coatings, Thin Solid Films 377–378 (2000) 788–792, https://doi.org/10.1016/S0040-6090(00)01452-8.

[23] I.A. Fisher, Variables influencing the characteristics of plasma-sprayed coatings, Int. Metall. Rev. 17 (1) (1972) 117–129, https://doi.org/10.1179/imtlr.1972.17.1.117.

[24] M. Uma Devi, On the nature of phases in Al_2O_3 and Al_2O_3–SiC thermal spray coatings, Ceram. Int. 30 (4) (2004) 545–553, https://doi.org/10.1016/j.ceramint.2003.09.007.

[25] R.-S. Zhou, R.L. Snyder, Structures and transformation mechanisms of the η, γ and θ transition aluminas, Acta Crystallogr. B 47 (1991) 617–630, https://doi.org/10.1107/S0108768191002719.

[26] M.H. Sehhat, J. Chandler, Z. Yates, A review on ICP powder plasma spheroidization process parameters, Int. J. Refract. Metals Hard Mater. 103 (2022), 105764, https://doi.org/10.1016/j.ijrmhm.2021.105764.

[27] H. Fukanuma, R. Huang, Y. Tanaka, Y. Uesugi, Mathematical modeling and numerical simulation of splat cooling in plasma spray coatings, J. Therm. Spray Technol. 18 (5–6) (2009) 965–974, https://doi.org/10.1007/s11666-009-9366-6.

[28] S. Guessasma, G. Montavon, C. Coddet, Velocity and temperature distributions of alumina–titania in-flight particles in the atmospheric plasma spray process, Surf. Coating. Technol. 192 (1) (2005) 70–76, https://doi.org/10.1016/j.surfcoat.2004.03.020.

[29] G. Mohanty, J.M. Wheeler, R. Raghavan, J. Wehrs, M. Hasegawa, S. Mischler, L. Philippe, J. Michler, Elevated temperature, strain rate jump microcompression of nanocrystalline nickel, Phil. Mag. 95 (16–18) (2014) 1878–1895, https://doi.org/10.1080/14786435.2014.951709.

[30] W.C. Oliver, G.M. Pharr, Measurement of hardness and elastic modulus by instrumented indentation: advances in understanding and refinements to methodology, J. Mater. Res. 19 (1) (2004) 3–20, https://doi.org/10.1557/jmr.2004.19.1.3.

[31] Z. Károly, J. Szépvölgyi, Plasma spheroidization of ceramic particles, Chem. Eng. Process: Process Intensif. 44 (2) (2005) 221–224, https://doi.org/10.1016/j.cep.2004.02.015.

[32] L. Bianchi, A. Léger, M. Vardelle, A. Vardelle, P. Fauchais, Splat formation and cooling of plasma-sprayed zirconia, Thin Solid Films 305 (1–2) (1997) 35–47, https://doi.org/10.1016/S0040-6090(97)80005-3.

[33] R.B. Bagwell, G.L. Messing, Effect of seeding and water vapor on the nucleation and growth of a-Al_2O_3 from γ-Al_2O_3, J. Am. Ceram. Soc. 82 (4) (1999) 825–832, https://doi.org/10.1111/j.1151-2916.1999.tb01842.x.

[34] H.-J. Youn, J.W. Jang, I.-T. Kim, K, S, Hong, low-temperature Formation of α-alumina by doping of an alumina-sol, J. Colloid Interface Sci. 211 (1) (1999) 110–113, https://doi.org/10.1006/jcis.1998.5977.

[35] K. Sabiruddin, J. Joardar, P.P. Bandyopadhyay, Analysis of phase transformation in plasma sprayed alumina coatings using Rietveld refinement, Surf. Coating. Technol. 204 (20) (2010) 3248–3253, https://doi.org/10.1016/j.surfcoat.2010.03.026.

[36] S. Yılmaz, M. Ipek, G.F. Celebi, C. Bindal, The effect of bond coat on mechanical properties of plasma-sprayed Al_2O_3 and Al_2O_3–13 wt% TiO_2 coatings on AISI 316L stainless steel, Vacuum 77 (3) (2005) 315–321, https://doi.org/10.1016/j.vacuum.2004.11.004.

[37] D. Goberman, Y.H. Sohn, L. Shaw, E. Jordan, M. Gell, Microstructure development of Al_2O_3–13wt.%TiO_2 plasma sprayed coatings derived from nanocrystalline powders, Acta Mater. 50 (5) (2002) 1141–1152, https://doi.org/10.1016/S1359-6454(01)00414-1.

[38] M.L. Gualtieri, M. Prudenziati, A.F. Gualtieri, Quantitative determination of the amorphous phase in plasma sprayed alumina coatings using the Rietveld method, Surf. Coating. Technol. 201 (6) (2006) 2984–2989, https://doi.org/10.1016/j.surfcoat.2006.06.009.

[39] S. Costil, C. Verdy, R. Bolot, C. Coddet, On the role of spraying process on microstructural, mechanical, and thermal response of alumina coatings, J. Therm. Spray Technol. 16 (2007) 839–843, https://doi.org/10.1007/s11666-007-9081-0.

[40] R.J. Damani, A. Wanner, Microstructure and elastic properties of plasma-sprayed alumina, J. Mater. Sci. 35 (2000) 4307–4318, https://doi.org/10.1023/A:1004888419594.

[41] P. Gehre, C.G. Aneziris, EBSD- and CT-analyses for phase evolution and crack investigations of thermal shocked flame sprayed alumina and alumina-rich structures, Ceram. Int. 37 (6) (2011) 1731–1737, https://doi.org/10.1016/j.ceramint.2011.01.032.

[42] Z. Károly, J. Szépvölgyi, Hollow alumina microspheres prepared by RF thermal plasma, Powder Technol. 132 (2–3) (2003) 211–215, https://doi.org/10.1016/S0032-5910(03)00077-9.

[43] I. Gulyaev, Experience in plasma production of hollow ceramic microspheres with required wall thickness, Ceram. Int. 41 (1) (2015) 101–107, https://doi.org/10.1016/j.ceramint.2014.08.040.